

Research note

deblended-data reconstruction using generalized blending and deblending models

Ishiyama, Tomohide; Ali, Mohammed Y.; Ishikawa, Satoshi; Blacquiere, Gerrit; Nakayama, Shotaro

DOI

[10.1111/1365-2478.12801](https://doi.org/10.1111/1365-2478.12801)

Publication date

2019

Document Version

Final published version

Published in

Geophysical Prospecting

Citation (APA)

Ishiyama, T., Ali, M. Y., Ishikawa, S., Blacquiere, G., & Nakayama, S. (2019). Research note: deblended-data reconstruction using generalized blending and deblending models. *Geophysical Prospecting*, *67*(7), 1852-1866. <https://doi.org/10.1111/1365-2478.12801>

Important note

To cite this publication, please use the final published version (if applicable).
Please check the document version above.

Copyright

Other than for strictly personal use, it is not permitted to download, forward or distribute the text or part of it, without the consent of the author(s) and/or copyright holder(s), unless the work is under an open content license such as Creative Commons.

Takedown policy

Please contact us and provide details if you believe this document breaches copyrights.
We will remove access to the work immediately and investigate your claim.

Research note: deblended-data reconstruction using generalized blending and deblending models

Tomohide Ishiyama^{1*}, Mohammed Y. Ali², Satoshi Ishikawa³, Gerrit Blacquiere⁴ and Shotaro Nakayama⁴

¹ADNOC, P.O. Box 898, Abu Dhabi, United Arab Emirates, ²Khalifa University of Science and Technology, P.O. Box 2533, Abu Dhabi, United Arab Emirates, ³INPEX Corporation, Akasaka 5-3-1, Minato-ku, Tokyo 107-6332, Japan, and ⁴Delft University of Technology, Stevinweg1, 2628, CN Delft, The Netherlands

Received September 2018, revision accepted April 2019

ABSTRACT

We introduce a concept of generalized blending and deblending, develop its models and accordingly establish a method of deblended-data reconstruction using these models. The generalized models can handle real situations by including random encoding into the generalized operators both in the space and time domain, and both at the source and receiver side. We consider an iterative optimization scheme using a closed-loop approach with the generalized blending and deblending models, in which the former works for the forward modelling and the latter for the inverse modelling in the closed loop. We applied our method to existing real data acquired in Abu Dhabi. The results show that our method succeeded to fully reconstruct deblended data even from the fully generalized, thus quite complicated blended data. We discuss the complexity of blending properties on the deblending performance. In addition, we discuss the applicability to time-lapse seismic monitoring as it ensures high repeatability of the surveys. Conclusively, we should acquire blended data and reconstruct deblended data without serious problems but with the benefit of blended acquisition.

Key words: Blending, Deblending, Data processing, Generalized model, Inversion.

INTRODUCTION

In traditional acquisition, spatial and temporal interference between shots is avoided, often resulting in poor sampling in the source dimension. However, in blended acquisition, the interference is allowed, leading to dense and wide sampling in an economical way. Therefore, we can achieve higher data quality with lower survey time and cost by blending and deblending, that is blended acquisition followed by deblended-data-reconstruction processing. The blending and deblending, or simultaneous sourcing methodology is a leading-edge technology that is becoming common wisdom in the industry today, for example slip-sweep (Rozemond 1996); distance-separated simultaneous sweeping or shooting (Bouska 2010;

Ishiyama, Mercado and Belaid 2012); independent simultaneous sourcing (Howe *et al.* 2008); managed sources and spread (Bagaini, Daly and Moore 2012). There are plenty of examples using some concepts of this methodology; however, these are under certain constraints such as large distance separation among shot locations and large time shifts among shot times, thereby so far not fully enjoy the benefits of this methodology. Besides, several oil and gas companies, service companies and academics are developing autonomous sources and receivers in order to realize autonomous acquisition using these robots (seismic robotization, Berkhout 2012), which is promoting this methodology more and more.

As for blending at the source side, first, blended acquisition stands for continuous recording of seismic responses from incoherent shooting, the properties of which are characterized and encoded by random spatial distribution and

*E-mail: tmishiyama@adnoc.ae, tomohide.ishiyama@inpex.co.jp

time shifts among the involved sources of blended-source array (Berkhout 2008). The benefit of blended acquisition is to acquire a larger amount of data in a more economical way than traditional acquisition. In addition, this method offers denser and wider spatial sampling with finer intervals and larger apertures, thus broader spatial bandwidth than traditional one. Furthermore, this method allows potential improvement of signal-to-noise ratio because of less background noise recorded in a shorter survey-time window (Berkhout and Blacquiere 2013). Second, blended acquisition uses seismic responses from inhomogeneous shooting, in which the blended-source array consists of different sources rather than traditional equal ones, for example several types of narrow frequency-banded device instead of a certain type of broad frequency-banded one (dispersed source array or DSA, Berkhout 2012). This method yields frequency-banded wavefields generated by each shot, thereby offers multi-scale spatial sampling, for example optimally coarser spatial sampling for a low frequency source, whereas relatively denser spatial sampling for a high frequency one in order to meet the Shannon–Nyquist sampling theorem for each frequency band. Third, blended acquisition also uses signaturing, in which each source is encoded with its own signature, for example popcorn-shooting sequences (Abma and Ross 2013) and near-orthogonal firing sequences (Mueller *et al.* 2016) for marine acquisition; various sweeps (Bagaini 2006) and pseudo-random sweeps (Dean 2014) for land. This method again yields distinguishable wavefields generated by each shot. However, the trade-off against these methods is obviously that shot-generated wavefields are spatially and temporally overlapped and interfered with each other. Therefore, the blended data should be deblended, that is deblended data should be reconstructed in the course of processing after the blended acquisition.

Another concept in this methodology, in particular at the receiver side, is spatial sampling based on compressive sensing (Baraniuk 2007). This method introduces non-uniform and under-sampling acquisition followed by regularization and interpolation processing (Herrmann 2010; Mosher *et al.* 2014). The benefit is that a signal can be recovered from far fewer samples than required by the Shannon–Nyquist sampling theorem. The trade-off is the effort for regularization and interpolation. This is achieved by reconstructing from observed data on an irregular and coarse observed grid (on which the data are acquired) into the corresponding data on a regular and fine nominal grid (on which the data are reconstructed) in the measurement domain (e.g. the space-time domain). The spatial bandwidth to be recovered can be

arbitrarily determined according to the spatial sampling intervals and apertures of the nominal grid.

Combined implementation of these methods can enhance the blending and deblending methodology, make it more flexible with less constraint, thereby promote this methodology further for future seismic robotization. In this paper, we introduce a concept of generalized blending and deblending, and establish its models including all the above-mentioned means. Accordingly, we establish a method of deblended-data reconstruction using these models. We give an overview of the theory and method, and show existing real data examples in order to demonstrate its virtues. We discuss the complexity of blending properties on the deblending performance. In addition, we discuss the application to time-lapse seismic monitoring as it ensures high repeatability of the surveys.

GENERALIZED BLENDING AND DEBLENDING

A concept of generalized *blending* includes random encoding both in the space and time domain, both at the source and receiver side (e.g. double blending, Berkhout, Blacquiere and Verschuur 2009), thus all the above-mentioned means. In fact, incoherent and inhomogeneous shooting and signaturing are special cases of blending only at the source side; non-uniform and under sampling are special cases of blending with randomizing only in the space domain. Similarly, a concept of generalized *deblending* includes data reconstruction that works all for shot-generated-wavefields separation, spectrum recovery and balancing, designature, regularization and interpolation, again both at the source and receiver side.

For these generalized concepts, we do face a challenging question: how to fully reconstruct deblended data from the fully generalized blended data. We should solve this problem in order to fully enjoy the benefits of blending and deblending methodology. To address this challenge, we consider an iterative optimization algorithm using a closed-loop approach (Berkhout 2013). This approach has been developed for several stages in seismic processing, in which an optimal parameterization at each stage is used to describe its forward and inverse models. For deblended-data reconstruction, we use the properties of blended signal. Here, blended acquisition is encoded by the blending operators containing the shot locations, times, signatures, etc. for the involved sources of blended-source array. One of the properties is the coherency of blended signal versus the incoherency of blending noise in the pseudo-deblended domain (i.e. the domain after the adjoint of blending operation has been applied). This can be

posed as an inverse problem with quantifying the coherency and its solutions by selecting optimal metrics of the coherency. A key element is the sparse representation of the metrics, thus the model parameters in a transform domain, where blended signal is sparsely compressed, whereas blending noise is randomly distributed, for robust parameter selection or signal extraction. Examples are: Mahdad, Doulgeris and Blacquiére (2011) in the Fourier domain; Ibrahim and Sacchi (2014) in the Radon domain; Lin and Herrman (2009) in the curvelet domain; Kontakis and Verschuur (2014) in the focal domain.

THEORY AND METHOD

To describe seismic data, we introduce the WRW model for blending (Berkhout 2008; Berkhout *et al.* 2009). In this model, seismic events can be described for each monochromatic component by operator matrices. Each matrix multiplication represents a multi-dimensional spatial convolution, and each element of every matrix contains amplitude and phase information. Using this representation and the same mathematical notation, we can describe a forward model as

$$\mathbf{P}'' = \mathbf{\Gamma}_D \mathbf{P} \mathbf{\Gamma}_S, \quad (1)$$

$$\mathbf{P} = \mathbf{L}^H \mathbf{M}, \quad (2)$$

where \mathbf{P}'' is the blended data on an observed grid, \mathbf{P} is the unblended data on a nominal grid, both in the measurement domain. $\mathbf{\Gamma}_S$ and $\mathbf{\Gamma}_D$ are the generalized blending operators (i.e. the generalized shooting operator at the source side and the generalized sensing operator at the receiver side). The forward model corresponds to the generalized blending operation. This can include random encoding both in the space and time domain by specifying the locations, times, signatures, etc., thus can explain all incoherent and inhomogeneous shooting, signaturing, non-uniform and under sampling, each at the source and receiver side. Incoherent and inhomogeneous sensing can also be included theoretically at the receiver side, but might not be practical in real situations. Unless otherwise mentioned, we assume non-blending at the receiver side (i.e. $\mathbf{\Gamma}_D = \mathbf{I}$) in this paper. \mathbf{M} is the data in a transform domain (e.g. the Fourier domain). \mathbf{L} is the transform operator, and \mathbf{L}^H is the adjoint of \mathbf{L} where the superscript H denotes Hermitian (i.e. conjugate transpose). Similarly, we can describe an inverse model as

$$\mathbf{\Gamma}_D^H \mathbf{P}'' \mathbf{\Gamma}_S^H = \langle \mathbf{P} \rangle, \quad (3)$$

$$\mathbf{L} \langle \mathbf{P} \rangle = \langle \mathbf{M} \rangle, \quad (4)$$

where the angle bracket $\langle \cdot \rangle$ denotes estimated data. The inverse model corresponds to the generalized deblending operation. This is data reconstruction that can include all shot-generated-wavefields separation, spectrum recovery and balancing, designature, regularization and interpolation again each at the source and receiver side. However, this is an ill-posed problem since the inverse model is underdetermined (i.e. \mathbf{P}'' has less data than \mathbf{P}) and the generalized blending operators are not orthogonal (i.e. $\mathbf{\Gamma}_D^H \mathbf{\Gamma}_D \neq \mathbf{I}$, $\mathbf{\Gamma}_S \mathbf{\Gamma}_S^H \neq \mathbf{I}$) in general, which requires additional constraints in order to solve the problem. In these models, the blended data for a basis function, \mathbf{P}'' , is parameterized by the samples in the transform domain, \mathbf{M} .

Given these models and the observed data, \mathbf{P}'' , our goal is then to solve for the model parameters, \mathbf{M} , and the reconstructed data, $\mathbf{P}(\mathbf{M})$. We can describe the inverse problem as minimizing the objective function

$$J = \|\mathbf{P}'' - \langle \mathbf{P}'' \rangle\|_2^2 + \mu \sum_l \ln(1 + m_l^2 / \sigma^2), \quad (5)$$

where the first term on the right is the residual term, the second one is the regularization term with Cauchy norm. μ is a weighting factor related to a measure for noise present in the observed data. σ is a weighting factor for the model parameters specifying a degree of sparseness in the solution. \mathbf{m} is a column vector to represent \mathbf{M} in a lexicographic order. The subscript l denotes a number of samples. For instance, if certain samples in the transform domain, $\langle \mathbf{M} \rangle$, are the solution in the equation (5), $\langle \mathbf{P}_M \rangle = \mathbf{L}^H \langle \mathbf{M} \rangle$ is the deblended data on the nominal grid, and then $\langle \mathbf{P}'' \rangle = \mathbf{\Gamma}_D \langle \mathbf{P}_M \rangle \mathbf{\Gamma}_S$ is the reblended data on the observed grid in the measurement domain. The spatial sampling intervals and apertures of the nominal grid can be arbitrarily determined.

To solve the inverse problem, we introduce a closed-loop approach. Figure 1 illustrates the conceptual flow. The closed loop contains not only the inversion module (steps in blue in the figure) but also the forward-modelling module (steps in red in the figure), allowing evaluation of the residual between observed and estimated data, $\Delta \mathbf{P}'' = \mathbf{P}'' - \langle \mathbf{P}'' \rangle$, thus feedback from the estimated model parameters, $\langle \mathbf{M} \rangle$, via the estimated data, $\langle \mathbf{P}'' \rangle$. For our closed-loop approach, the transform domain is a three-dimensional Fourier domain, or more specifically the $k_D k_S f$ domain, where k_D and k_S represent the wavenumbers each in the receiver and source dimension, and f for the frequency. The blended signal is more sparsely compressed in this domain, rather than in a conventional Fourier domain. For the parameter selection, we adopt a pre-conditioning followed by a regularization-term

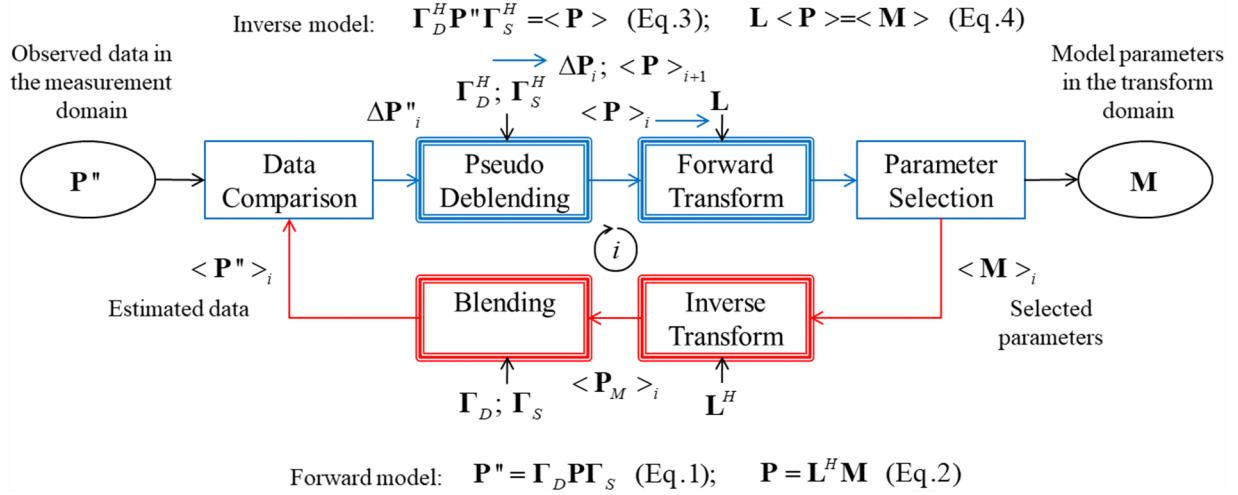


Figure 1 Conceptual flow of the closed-loop approach for deblended-data reconstruction.

algorithm of iterative reweighted least-squares inversion, instead of our previous thresholding algorithm (Ishiyama *et al.* 2018). The pseudo-deblended data are pre-conditioned by a velocity filtering in the $k_D k_S$ - f domain. A wide-band filtering with a low velocity is used to pass all blended signal in our case. Optionally, a narrow-band filtering with a high velocity is used during early iterations, and its pass band is extended gradually in the course of iterations. The model parameters are then updated under sparsity constraints promoted by the regularization term so that the objective function is oriented to the minimum. This algorithm also helps the process avoid overfitting and makes it stable. We select Cauchy norm rather than L1 and L2 norms for the regularization term since this norm works the best compared to other norms in our case (Ishikawa *et al.* 2018). Optimal μ and σ should be selected by processing-parameter testing for each dataset. μ is first estimated and fixed around the order of $\max(|\mathbf{P}'|)^2$, and σ is then fine-tuned in the order of $10^{-3} \max(|\langle \mathbf{M} \rangle|)$ in our case.

For each iteration of the closed loop, from certain estimated deblended data, $\langle \mathbf{P} \rangle_i$, the model parameters are updated in the Fourier domain

$$\langle \mathbf{m} \rangle_i = (\mathbf{L}\mathbf{L}^H + \mu\mathbf{Q}(\mathbf{m}_i))^{-1} \mathbf{m}_i, \quad (6)$$

where

$$\mathbf{m}_i = \mathbf{L} \langle \mathbf{p} \rangle_i, \quad (7)$$

$$\mathbf{Q}(\mathbf{m}_i) = \begin{pmatrix} Q(m_{i,1}) & & & \\ & \ddots & & \\ & & Q(m_{i,l}) & \\ & & & \ddots \end{pmatrix},$$

$$\mathbf{Q}(m_{i,l}) = (\sigma^2 (1 + m_{i,l}^2/\sigma^2))^{-1}, \quad (8)$$

that is $\mathbf{Q}(\mathbf{m}_i)$ is a diagonal matrix to include damping factors for the model parameters. Note that \mathbf{Q} is \mathbf{m} dependent, allowing $\langle \mathbf{m} \rangle$ to become sparse. $\langle \mathbf{p} \rangle_i$ is a column vector to represent $\langle \mathbf{P} \rangle_i$ in a lexicographic order. The subscript i denotes a number of iterations. Equation (7) corresponds to the equation (4). Then, from $\langle \mathbf{M} \rangle_i$ and $\langle \mathbf{P}_M \rangle_i$ after the equation (2), the residual is updated:

$$\begin{aligned} \Delta \mathbf{P}_i &= \Gamma_D^H (\mathbf{P}'' - \Gamma_D \langle \mathbf{P}_M \rangle_i \Gamma_S) \Gamma_S^H \\ &= \Gamma_D^H (\mathbf{P}'' - \langle \mathbf{P}'' \rangle_i) \Gamma_S^H \\ &= \Gamma_D^H \Delta \mathbf{P}_i' \Gamma_S^H, \end{aligned} \quad (9)$$

by referring to the equations (1) and (3). Finally, the estimated deblended data are updated:

$$\langle \mathbf{P} \rangle_{i+1} = \langle \mathbf{P} \rangle_i + \alpha_i \Delta \mathbf{P}_i, \quad (10)$$

where α_i is a scale factor to orient the residual to the minimum; a step length in a steepest decent algorithm in our case (Nakayama *et al.* 2018). This update is the input for the next iteration. This loop process is iterated until it has reached a stopping criterion. At the convergence, $\langle \mathbf{P} \rangle_{i+1}$ becomes mostly the same as $\langle \mathbf{P}_M \rangle_i$ since $\Delta \mathbf{P}_i$ becomes nearly zero.

Figures 2 and 3 step-by-step illustrate the closed loop using a blended dataset with two sources in the blended-source array, which will be described in detail and used again in the following section. Figure 2 shows the illustration in the space-time domain for display purpose. Figure 2(a,b) shows the input, thus the blended data, \mathbf{P}'' , in the (common-source and) common-receiver domain. For the first iteration, the pseudo-deblended data, $\langle \mathbf{P} \rangle_p$, corresponds to the first

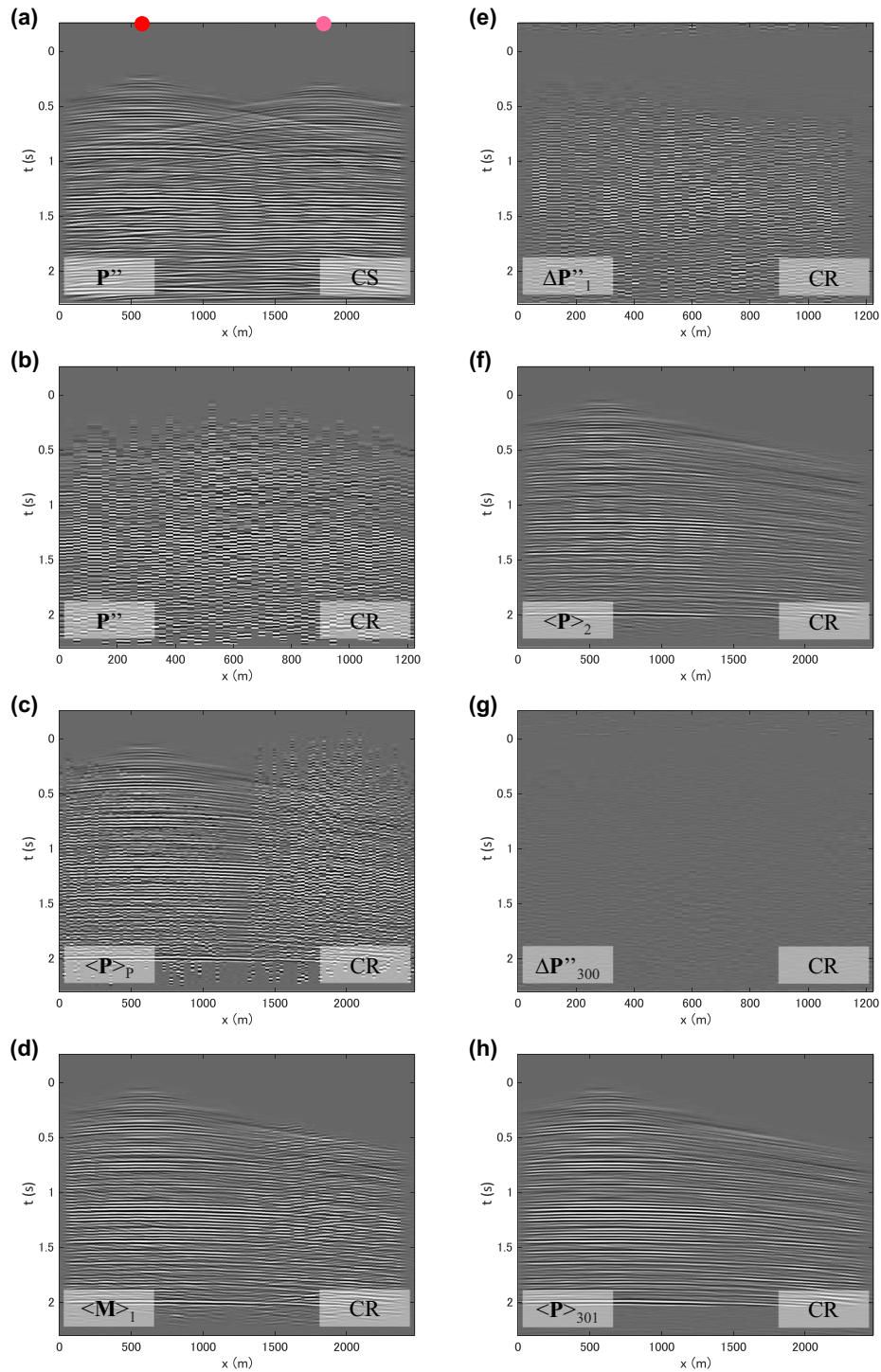


Figure 2 Step-by-step illustration of the closed-loop: (a) and (b) blended data; (c) pseudo-deblended data; (d) estimated model parameters; (e) and (g) residual; (f) and (h) estimated deblended data in the common-source (CS) and common-receiver (CR) domain. Illustrations (c)–(f) for the first iteration; (g) and (h) after 300 iterations. The red and magenta circles indicate the two sources and their shot locations of blended-source array in this particular section. In the blended domain, the blended shots are sorted along the first sources and their shot locations, thereby the spatial sampling aperture is halved in the CR domain.

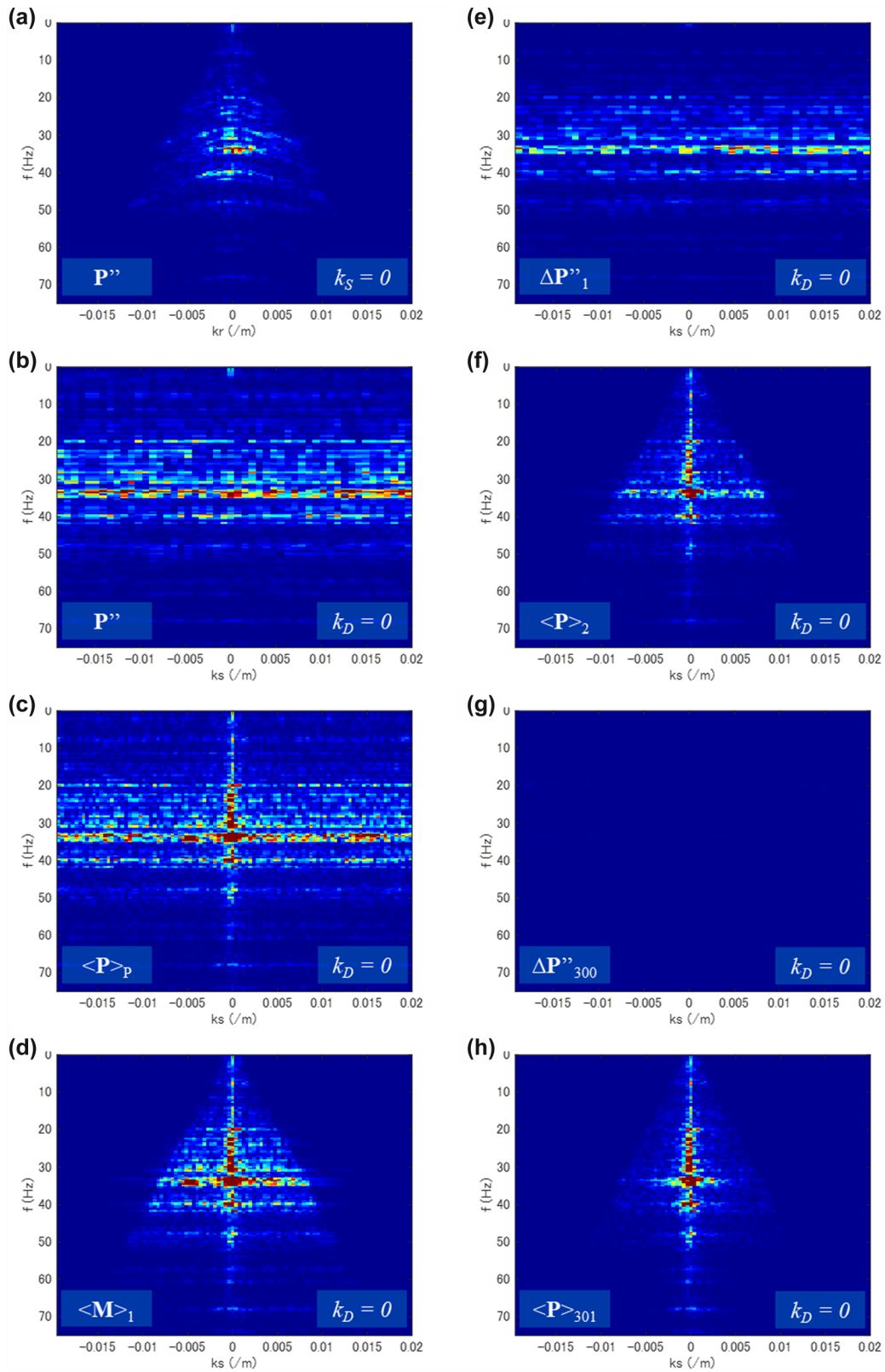


Figure 3 The same illustration as Fig. 2 but in the $k_D k_S$ - f domain.

estimated deblended data, $\langle \mathbf{P} \rangle_1$ (Fig. 2c). The model parameters, $\langle \mathbf{M} \rangle_1$, are updated by the pre-conditioning followed by the regularization-term algorithm (Fig. 2d). The residual, $\Delta \mathbf{P}'_1$, and the estimated deblended data, $\langle \mathbf{P} \rangle_2$, are updated by the closed-loop algorithm (Fig. 2e,f). This loop process is iterated up to a stopping criterion, for example $\Delta \mathbf{P}'_{300}$ and $\langle \mathbf{P} \rangle_{301}$ (Fig. 2g,h). Figure 3 shows the same illustration as Fig. 2 but in the $k_D k_S f$ domain again for display purpose.

EXAMPLES

We demonstrate our method of deblended-data reconstruction with existing 2-D 2-C OBC data acquired in a shallow-water environment offshore Abu Dhabi. The target levels are Lower Cretaceous and Upper Jurassic successions, around 1.5 s in the seismic data. The number of shot points is trimmed to 100, and 100 for receiver points as well. The spatial sampling intervals and apertures are 25 m and 2500 m, respectively, both for the sources and receivers. First, pre-processing was applied, such as random and linear noise attenuation and P-Z summation. The consequent data are regarded as traditional unblended data, \mathbf{P} . Then, blended data, \mathbf{P}' , were numerically synthesized with several blending scenarios. These data correspond to noise-attenuated blended data. This is based on the fact that there are several noise-attenuation techniques that can be applied to non-uniform and under-sampled blended data beyond aliasing and before deblending (e.g. Ishiyama *et al.* 2016). For the synthesizing process, the blending fold (i.e. the number of involved sources in blended-source array) is 2. The maximum spatial separation is 1250 m, and the maximum random time shift is 0.256 s. This assumes a difficult situation with a small separation of distance offsets and time shifts between the shots in blended-source array. The amplitude level is similar among the shots. Different amplitude levels, though, can be treated by including corresponding scale factors in the generalized deblending model, for example a scale factor of 0.5 for two times larger amplitudes. The blending scenarios, represented by generalized blending operators Γ_S and Γ_D for each case, are as follows:

1 Incoherent shooting only at the source side.

For marine,

2 Popcorn, or self-inhomogeneous shooting at the source side in addition to the scenario 1, by using three types of frequency-banded airguns in popcorn-shooting configuration for each shot: low-frequency-banded subunit of 0/4-12/20 Hz; mid of 8/16-24/40 Hz; high of 16/32-96/125 Hz, with random and multi-scale shot repetition by activating the subunits successively over a period of time rather than firing those at the same

time as a tuned one: 1 of 9 repetitions for low; 2 for mid; 6 for high.

3 Inhomogeneous shooting at the source side in addition to the scenario 1, by using three types of frequency-banded airguns in marine DSA: low-frequency-banded source of 0/4-12/20 Hz; mid of 8/16-24/40 Hz; high of 16/32-96/125 Hz, with random spatial distribution and multi-scale spatial sampling: 11% of 100 shot points for low; 22% for mid; 67% for high.

The scenarios 2 and 3 are primarily for stationary acquisition geometries. These scenarios, though, could be also for streamer acquisition with an assumption of minimal influence from the non-stationarity.

For land,

4 Inhomogeneous sweeping at the source side in addition to the scenario 1, by using three types of frequency-banded vibrators in land DSA with the array configuration same as for the scenario 3. The sweep length is 6.5 s each with its own sweep rate.

For transition zone,

5 Combined case of the scenarios 1, 3 and 4, with random spatial distribution: 50% of 100 shot points for airguns of marine DSA; 50% for vibrators of land DSA.

6 Fully generalized case of the scenario 5 in addition to non-uniform and under sampling both at the source and receiver side (i.e. $\Gamma_D \neq \mathbf{I}$ in terms of sampling), by applying 9% random decimation each at the source and receiver side, consequently about 25% random decimation in total.

The sequent figures show six examples with the blending scenarios 1–6, respectively, followed by deblended-data reconstruction. Figures 4 and 5 show the first example. The first column shows the inputs including the blended data, \mathbf{P}' , in the common-source (and common-receiver) domain. The red and magenta circles indicate the two sources and their shot locations of blended-source array in this particular section. For the pseudo-deblended data in the first iteration, $\langle \mathbf{P} \rangle_p$, the blended signal is coherent but the blending noise is incoherent in the common-receiver domain, indicating that the coherency is effectively promoted in this domain. The second column shows the outputs including the deblended data, $\langle \mathbf{P} \rangle$, after 300 iterations. In addition to the residual between blended and reblended data, $\Delta \mathbf{P}' = \mathbf{P}' - \langle \mathbf{P}' \rangle$, the difference between unblended and deblended data, $\Delta \mathbf{P}_N = \mathbf{P} - \langle \mathbf{P} \rangle$, can be displayed since the unblended data, \mathbf{P} , are known here. This also makes it possible to estimate the signal-to-noise ratio (S/N), $\mathbf{P}/\Delta \mathbf{P}_N$, besides the residual, $\Delta \mathbf{P}'/\mathbf{P}'$. The residual significantly improved 24 dB down and the S/N consequently rose 19 dB up. The same results are observed in terms of

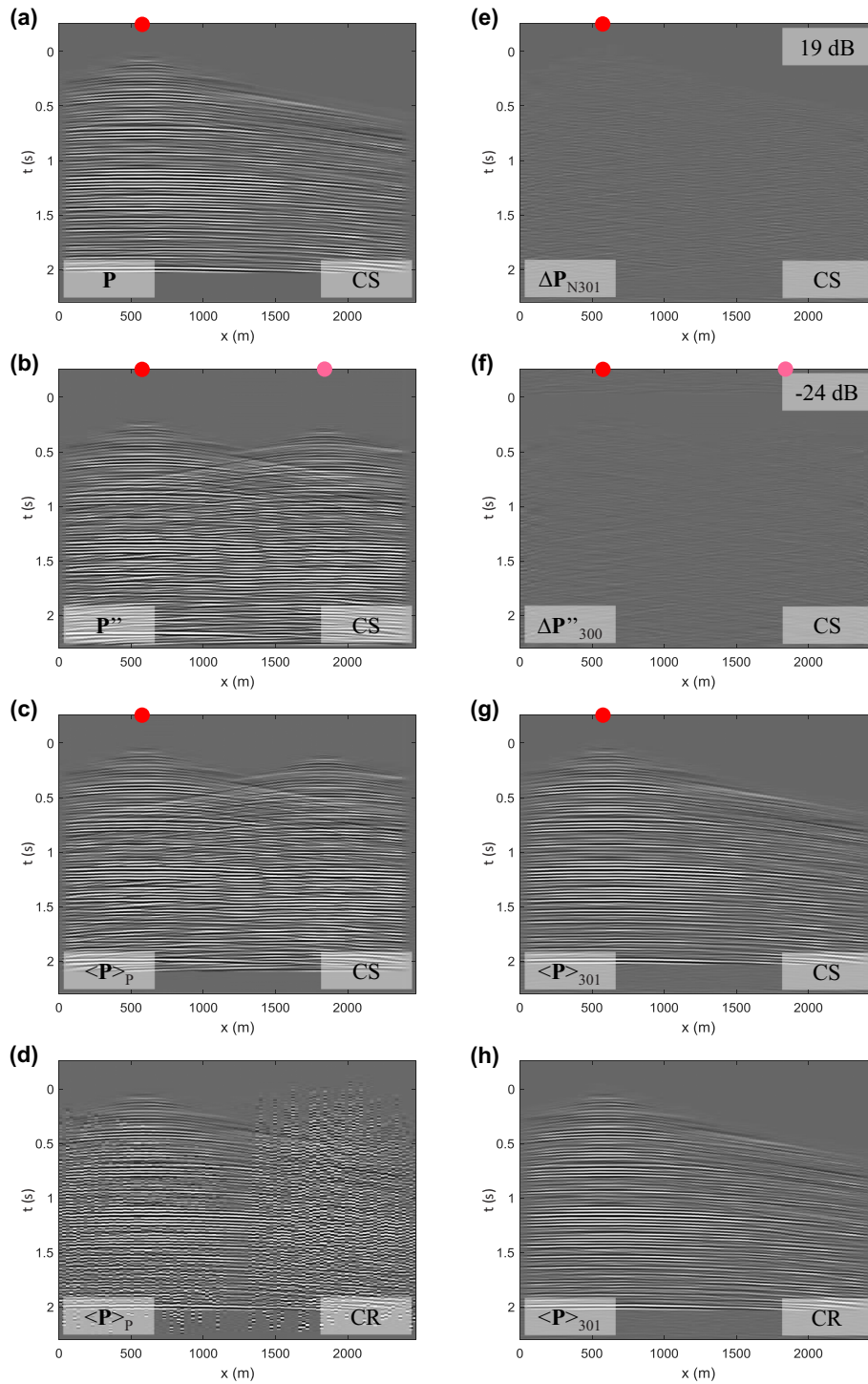


Figure 4 Results for the blending scenario 1. Inputs: (a) unblended data; (b) blended data; (c) and (d) pseudo-deblended data in the CS and CR domain. Outputs after 300 iterations: (e) difference between (a) and (g) with the S/N value; (f) residual between (b) and rebled data of (g) with its value; (g) and (h) deblended data each in the CS and CR domain. The red and magenta circles indicate the two sources and their shot locations of blended-source array in this particular section. The unblended data were originally tapered at the edges both in the CS and CR domain. This results in some imprints in other domains, for example the blending noise is not so visible around the middle for the pseudo-deblended data in the CR domain, though this might not badly affect the examples.

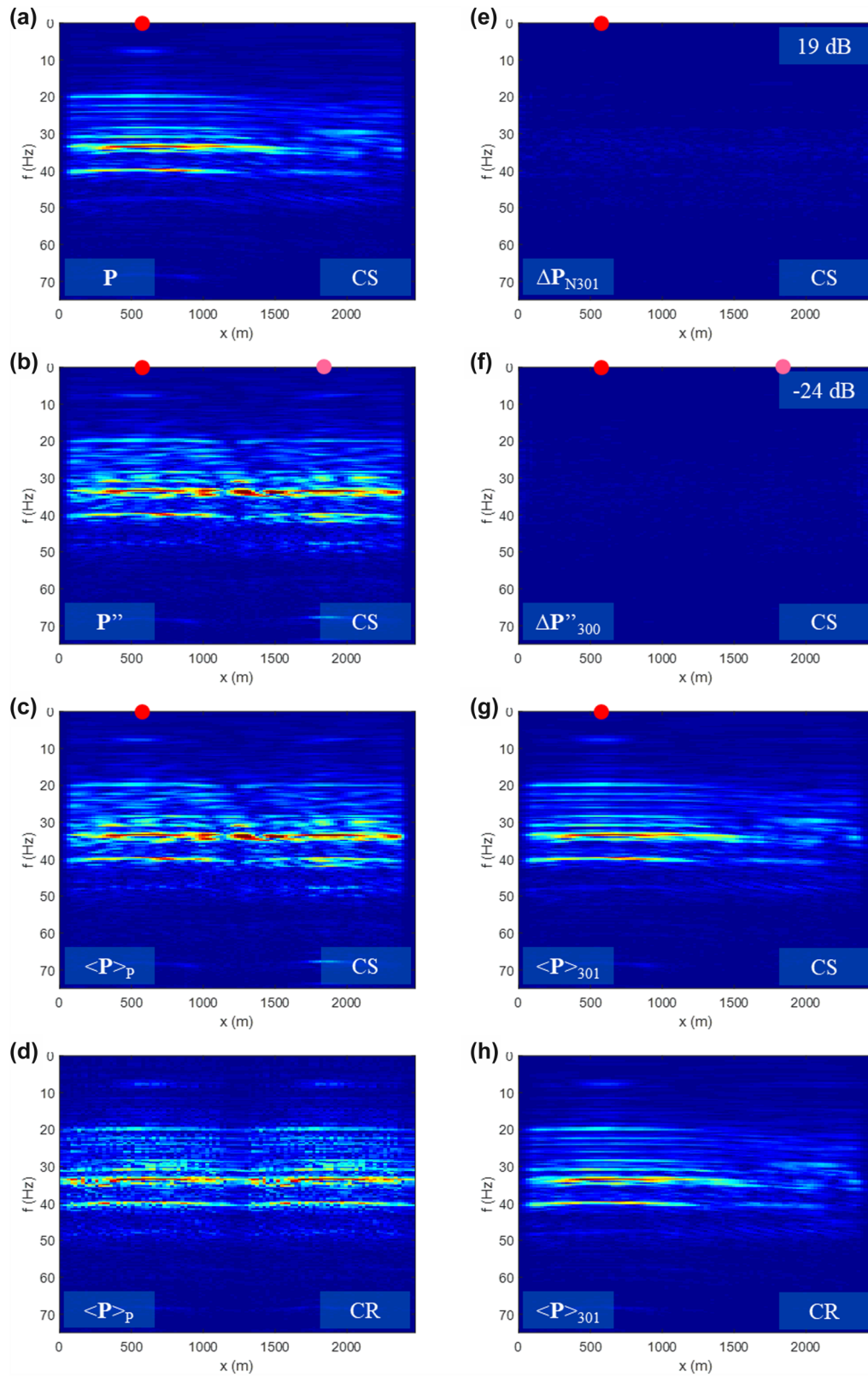


Figure 5 The same results as Fig. 4 but in the space-frequency domain.

the temporal spectrum in the space-frequency domain. This demonstrates that our method successfully reconstructed the deblended data from the blended data, in particular separated the interfered shot-generated wavefields quite well.

Figure 6 shows examples 2–5. The blended data, P' , at the second row and the deblended data, $\langle P \rangle$, after 300 iterations with the S/N value at the fourth row; see Fig. 4(a) for comparison with the unblended data, P . The two generalized blending operators, Γ_S , are shown at the first row for the red one and at the third row for the magenta one in this particular section. Examples 3 and 4 (Fig. 6b,c) indicate that our method well reconstructed the full-frequency deblended data from the blended data shot by the narrow frequency-banded sources in DSA, thus it entirely recovered and balanced the temporal spectrum correspondingly by interpolating data in each frequency band and combining those as the full frequency band. Moreover, examples 2 and 4 (Fig. 6a,c) indicate that our method properly reconstructed the designated deblended data from the signed blended data. For example 2 (Fig. 6a), our method restored notches caused by popcorn shooting, thus it again recovered and balanced the temporal spectrum by using information from nearby data. Furthermore, example 5 (Fig. 6d) indicates that our method simultaneously handled the blended data shot both by airguns and vibrators in DSA.

Figures 7 and 8 show the last example in the order same as for Figs 4 and 5. This is a fully generalized case so that all the results are observed again, in particular, those for spectrum recovery and balancing in the space-frequency domain. For the inputs, the unblended data (Fig. 8a) own the full frequency band; the blended data (Fig. 8b) have the mid and high frequency bands both from the red and magenta sources in DSA in this particular section; the pseudo-deblended data (Fig. 8c) have only the high frequency band from the red source there. Nevertheless, the outputs (Fig. 8e–h) show that our method entirely recovered and balanced the temporal spectrum. In addition, this reveals that our method nicely reconstructed the regularized and interpolated deblended data from the non-uniform and under-sampled blended data. This is clearly observed in terms of the temporal spectrum again in the space-frequency domain. For all the examples, the S/N resulted in more than 16 dB up, which is quite acceptable in general in seismic processing. This demonstrates that our method successfully worked even for the complicated blending situations without seriously affecting the deblending performance. Conclusively, our method fully reconstructed the deblended data from the fully generalized blended data, thus it totally and simultaneously achieved all shot-generated-wavefields

separation, spectrum recovery and balancing, signature, regularization and interpolation both at the source and receiver side.

DISCUSSIONS

The above examples show that our method works even for complicated blending situations encoded by the complicated generalized blending operators. We discuss the influence of complexity on the deblending performance and a way forward on this matter. First, the blending properties are arbitrarily preset, or known acquisition parameters, thereby can be encoded precisely in the operators. The complexity of blending properties increases the uniqueness of shots in blended-source array, which allows more straightforward shot-generated wavefields separation and signature by decoding the operators, or deconvolving the signatures by the inverse operation. Remember that the examples use blended data numerically synthesized by the operators, thereby there is no difference between real signatures and preset ones in the operators. However, it is not a case in general for real blended data. The difference of real signatures from preset ones might appear, and affect the deblending performance, though this could be remedied by the iterative optimization scheme in our method. We will address this concern in our ongoing study by analysing sensitivity to the difference.

Second, though the complexity of blending properties allows more simple and robust operations for shot-generated-wavefields separation and signature, this leads to more challenging situations for spectrum recovery and balancing, regularization and interpolation. There is a trade-off: more complicated generalized blending operators improve the former operations, but make the latter ones more difficult. For instance, for a simple case (e.g. example 1), the shot-generated wavefields are overlapped and interfered with each other even after the pseudo-deblending (Fig. 4c). Besides, for a complicated case (e.g. example 6), pseudo-deblended are the designated and frequency-banded wavefields, corresponding to filtering results naturally in the frequency domain (Fig. 7c). This is then switched to a data-reconstruction problem for spectrum recovery and balancing, corresponding to regularizing, interpolating data in each frequency band and combining those as the full frequency band. This is solved by the iterative optimization scheme in our method. The resulting signal-to-noise ratio is a bit lower than that of the simple case in these examples.

Third, the number of sources in blended-source array was set as 2, and all the blending scenarios achieved deblending

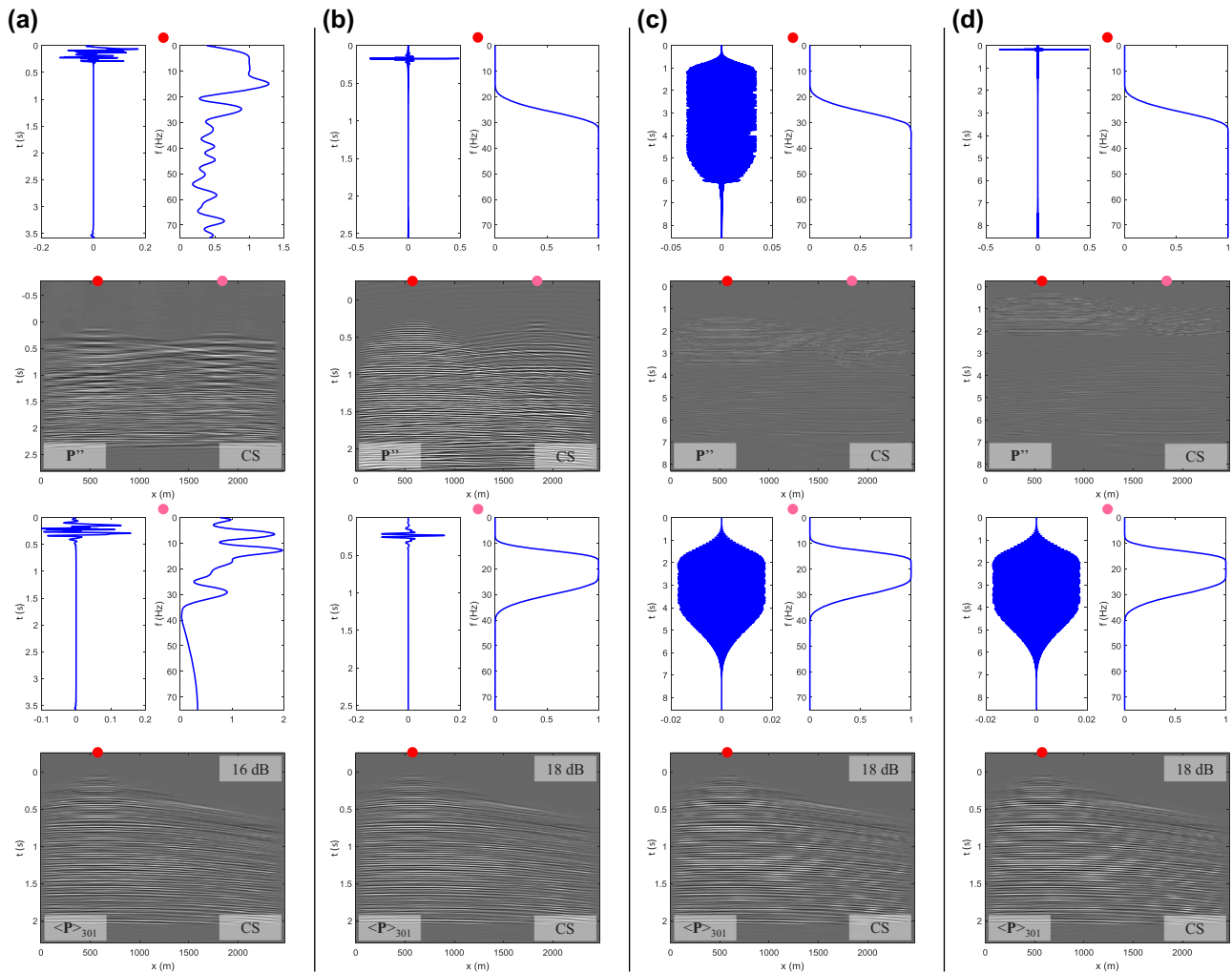


Figure 6 Results for the blending scenarios 2–5: (a) scenario 2 of marine popcorn-shooting case; (b) scenario 3 of marine DSA case; (c) scenario 4 of land DSA case; (d) scenario 5 of a combined case of TZ DSA. Blended data at the second row and deblended data after 300 iterations with the S/N value at the fourth row; see Fig. 4(a) for comparison with the unblended data. The amplitudes of blended data are two times scaled for display purpose. The red and magenta circles indicate the two sources and their shot locations of blended-source array in this particular section. The two generalized-blending operators are shown at the first row for the red one and at the third row for the magenta one each in the time and frequency domain. The blended wavefields are shot by a high-frequency-banded source of the red one, and a mid-frequency-banded source of the magenta one for (b), (c) and (d); also shot by an airgun of the red one, and a vibrator of the magenta one for (d).

well in the examples. However, increasing the blending fold leads to poorer deblending in general. This is because the shot-generated wavefields are more severely overlapped and interfered with each other. The randomly scattered blending noise dominates and surpasses the sparsely compressed blended signal in the transform domain; consequently, the iterative optimization scheme often converges in local minima, and hardly reaches a stopping criterion in our method. Nevertheless, we feel in our ongoing study that a complicated case (e.g. more blending folds in example 6) can achieve successful deblending even in this difficult situation, though a simple case (e.g.

more blending folds in example 1) cannot. All the discussions come from the generalized blending and deblending models, which can explain any blending properties, or any blending methods. With this highly flexible and tolerant model, we do face a challenging question: what is an optimal blended-acquisition design that is the most suitable for deblended-data-reconstruction processing. We will address this challenge in our ongoing study by blended-acquisition designing based on the deblending performance. Furthermore, we will acquire a pilot blended data and reconstruct the deblended data in order to validate our method.

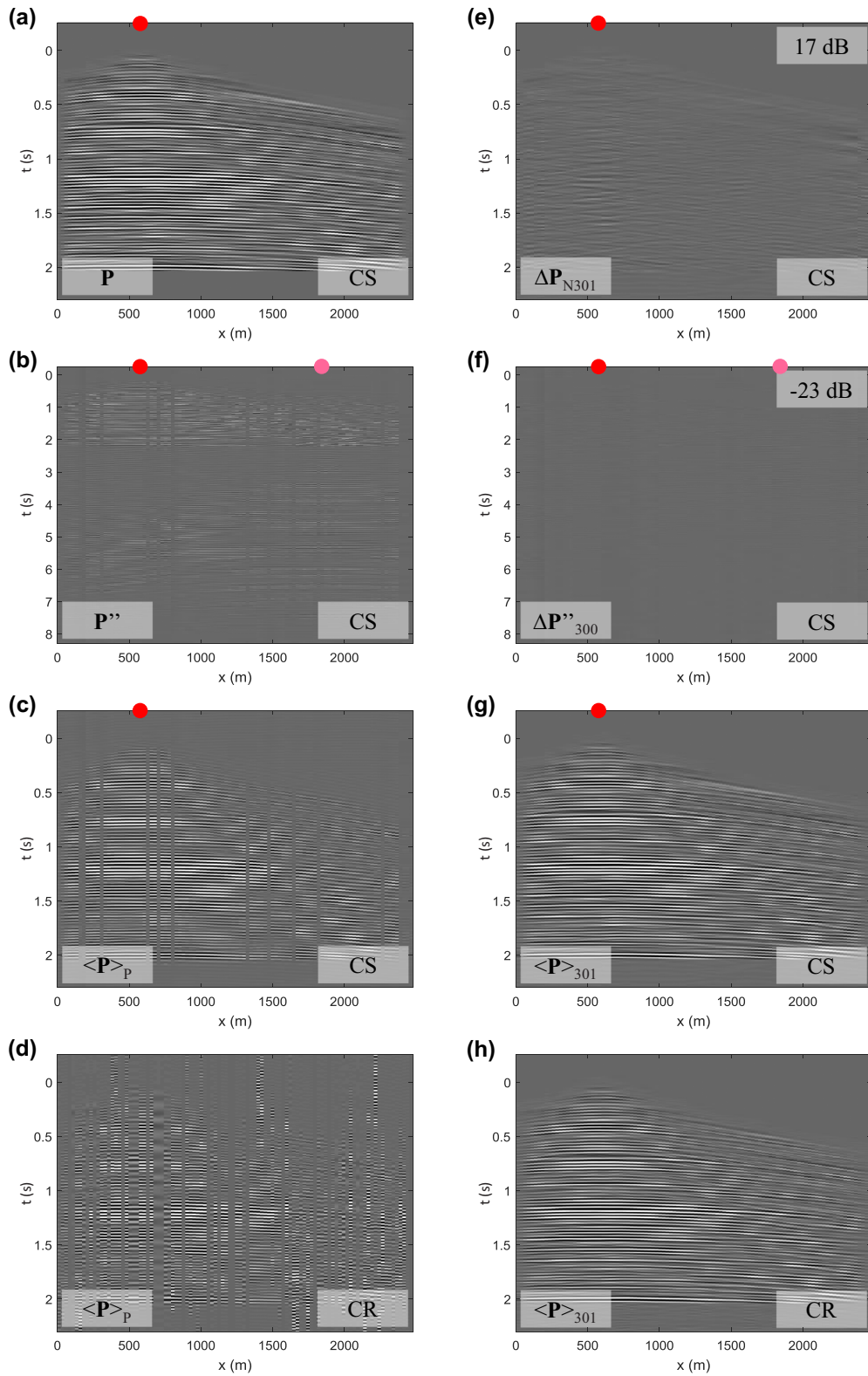


Figure 7 Results for the blending scenario 6 of a fully generalized case of TZ DSA in the order same as for Fig. 4. The amplitudes of (b) and (f) are two times scaled for display purpose. The blended wavefields are shot as same as for Fig. 6(d).

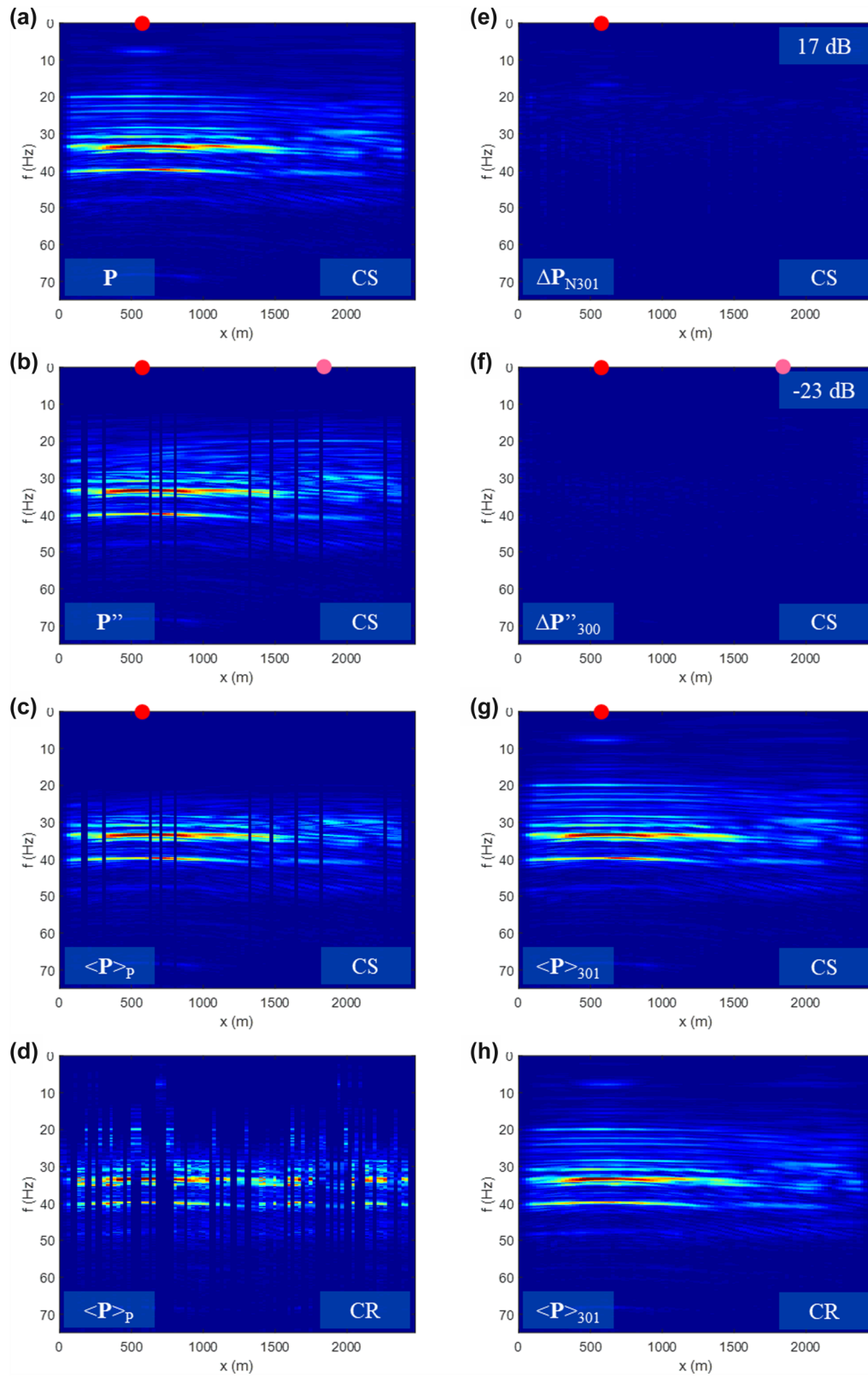


Figure 8 The same results as Fig. 7 but in the space-frequency domain.

Finally, we discuss the application of our methodology to time-lapse seismic monitoring as it ensures high repeatability of the surveys. The examples suggest that our methodology could be used for time-lapse seismic monitoring, which involves repeating surveys over an oil and gas field. The objective is to determine changes occurring in a reservoir in an intervening time, such as caused by hydrocarbon production or fluid injection. The results are commonly displayed as differences of seismic properties representing the changes in the reservoir like saturation and pressure. The difference is usually small, in particular in carbonate reservoirs. Detectability of seismic properties and repeatability of seismic surveys are of great importance in determining a true signal other than artifacts. To achieve high repeatability, monitor surveys should follow the design of the baseline survey, for example, positioning sources and receivers as the baseline survey, as far as possible. However, oil and gas fields often become congested after the baseline survey due to additional infrastructure like production facilities, pipelines and rigs, making it impossible to reoccupy the same source and receiver positions for monitor surveys. Furthermore, the design of the legacy survey often becomes poorer compared to best practices in the industry to be used for monitor surveys, making it also difficult that the design is completely identical on the baseline and monitor surveys. This situation makes it quite challenging to ensure high repeatability in time-lapse seismic monitoring. Nevertheless, using our methodology, we can reconstruct from blended data on an irregular observed grid of a monitor survey into corresponding deblended data on a regular and fine nominal grid, which is adaptable for the baseline survey. Therefore, our methodology could reduce the repeatability problem, in which reconstructing deblended data in monitor surveys is much more realistic and reliable than using and positioning sources and receivers exactly as the baseline survey. For instance, in the examples, suppose that unblended data, \mathbf{P} , are from a traditional baseline survey, and blended data, \mathbf{P}' , are from a generalized blended monitor survey. This suggests that our method can fully reconstruct deblended data, $\langle \mathbf{P} \rangle$, from the monitor survey, which is comparable with the unblended data from the baseline survey. Again, we will acquire a pilot blended survey in a time-lapse manner in order to validate our methodology.

CONCLUSIONS

We established generalized blending and deblending models and a method of deblended-data reconstruction using these models. Our methodology is quite practical, and can

handle real situations. Indeed, this can handle incoherent and inhomogeneous shooting, signaturing, non-uniform and under sampling both at the source and receiver side for generalized blending; besides, shot-generated-wavefields separation, spectrum recovery and balancing, designature, regularization and interpolation again both at the source and receiver side for generalized deblending. Our method of deblended-data reconstruction succeeded to fully reconstruct deblended data from the fully generalized blended data. Therefore, we should acquire blended data and reconstruct deblended data without serious problems but with the benefit of blended acquisition.

ACKNOWLEDGEMENTS

We thank ADNOC for their supports and permission to publish this paper. We also thank the anonymous reviewers for their valuable comments to improve this paper.

REFERENCES

- Abma R. and Ross A. 2013. Popcorn shooting: sparse inversion and the distribution of airgun array energy over time. 83rd SEG Annual meeting Technical Program, Expanded Abstracts.
- Bagaini C. 2006. Overview of simultaneous Vibroseis acquisition methods. 76th SEG Annual meeting Technical Program, Expanded Abstracts.
- Bagaini C., Daly M. and Moore I. 2012. The acquisition and processing of dithered slip-sweep vibroseis data. *Geophysical Prospecting* 60, 618–639.
- Baraniuk R.G. 2007. Compressive sensing. *IEEE Signal Processing Magazine* 24, 118–124.
- Berkhout A.J. 2008. Changing the mindset in seismic data acquisition. *The Leading Edge* 27, 924–938.
- Berkhout A.J. 2012. Blended acquisition with dispersed source arrays. *Geophysics* 77, A19–A23.
- Berkhout A.J. 2013. The road ahead in seismic processing. 83rd SEG Annual meeting Technical Program, Expanded Abstracts.
- Berkhout A.J. and Blacquiere G. 2013. Effect of noise in blending and deblending. *Geophysics* 78, A35–A38.
- Berkhout A.J., Blacquiere G. and Verschuur D.J. 2009. The concept of double blending: combining incoherent shooting with incoherent sensing. *Geophysics* 74, A59–A62.
- Bouska J. 2010. Distance separated simultaneous sweeping, for fast, clean, vibroseis acquisition. *Geophysical Prospecting* 58, 123–153.
- Dean T. 2014. The use of pseudorandom sweeps for vibroseis surveys. *Geophysical Prospecting* 62, 50–74.
- Herrmann F.J. 2010. Randomized sampling and sparsity: getting more information from fewer samples. *Geophysics* 75, WB173–WB187.

- Howe D., Foster M., Allen T., Taylor B. and Jack I. 2008. Independent simultaneous sweeping – a method to increase the productivity of land seismic crews. 78th SEG Annual meeting Technical Program, Expanded Abstracts.
- Ibrahim A. and Sacchi M.D. 2014. Simultaneous source separation using a robust Radon transform. *Geophysics* 79, V1–V11.
- Ishikawa S., Ishiyama T., Ali M., Nakayama S. and Blacquièrè G. 2018. Deblended-data reconstruction using a sparse inversion method with regularization term for further application of blended acquisition in the Middle-East area. 13th SEGJ International Symposium, Expanded Abstracts.
- Ishiyama T., Mercado G. and Belaid K. 2012. 3D OBC seismic survey geometry optimization offshore Abu Dhabi. *First Break* 30, 52–59.
- Ishiyama T., Blacquièrè G., Verschuur D.J. and Mulder W. 2016. 3-D surface-wave estimation and separation using a closed-loop approach. *Geophysical Prospecting* 64, 1413–1427.
- Ishiyama T., Ishikawa S., Ali M., Nakayama S. and Blacquièrè G. 2018. Deblended-data reconstruction using generalized blending and deblending models. 80th EAGE Conference & Exhibition, Expanded Abstracts.
- Kontakis A. and Verschuur D.J. 2014. Deblending via sparsity-constrained inversion in the focal domain. 76th EAGE Conference & Exhibition, Extended Abstracts.
- Lin T.T.Y. and Herrmann F.J. 2009. Designing simultaneous acquisitions with compressive sensing. 71st EAGE Conference & Exhibition, Extended Abstracts.
- Mahdad A., Doulgeris P. and Blacquièrè G. 2011. Separation of blended data by iterative estimation and subtraction of blending interference noise. *Geophysics* 76, Q9–Q17.
- Mosher C., Li C., Morley L., Ji Y., Janiszewski F., Olson R. and Brewer J. 2014. Increasing the efficiency of seismic data acquisition via compressive sensing. *The Leading Edge* 33, 386–391.
- Mueller M.B., Halliday D.F., Manen D.J. and Robertson J.O.A. 2016. Optimizing near-orthogonal air-gun firing sequences for marine simultaneous source separation. *Geophysics* 81, V415–V423.
- Nakayama S., Blacquièrè G., Ishiyama T. and Ishikawa S. 2018. Blended-acquisition design of irregular geometries towards faster, cheaper, safer and better seismic surveying. *Geophysical Prospecting*. Online published.
- Rozemond H.J. 1996. Slip-sweep acquisition. 66th SEG Annual meeting Technical Program, Expanded Abstracts.